



Morphology-controlled synthesis of MnO₂ grown on carbon fiber paper for high-rate supercapacitor electrode

Gaodan Luo¹, Guiqiang Diao², Qingqing He¹, Shengbo Han¹, Dai Dang¹, and Xiaohui Su^{1,*}

¹ School of Chemical Engineering and Light Industry, Guangdong University of Technology, Guangzhou 510006, Guangdong, China

² School of Chemistry and Materials Engineering, Huizhou University, Huizhou 516007, China

Received: 1 February 2022

Accepted: 29 June 2022

Published online:
12 July 2022

© The Author(s), under exclusive licence to Springer Science+Business Media, LLC, part of Springer Nature 2022

ABSTRACT

Nanostructured MnO₂ with different morphologies based on carbon fiber paper (CFP) had been successfully synthesized via a hydrothermal process. The emphasis of this report focuses on the effect of the Co doping content on the morphologies and electrochemical properties of as-obtained MnO₂ electrodes, thereby obtaining the optimal electrode material. Such optimal hierarchical porous nanoflowers entwined with nanowires architecture (Co-MnO₂/CFP-1) was obtained by a certain Co content, which displayed an excellent capacitive performance. The Co-MnO₂/CFP-1 electrode achieved a relatively high specific capacitance of 161 F g⁻¹ at 1 A g⁻¹, and 57% of the capacitance retention for Co-MnO₂/CFP-1 when the current density ranging from 1 to 8 A g⁻¹, which was 27 times than MnO₂ without Co doping (MnO₂/CFP), proving its excellent rate capability. The Co-MnO₂/CFP-1 electrode exhibited a prominent cycle stability of 98% in 10,000 cycles at 4 A g⁻¹. This significant improvement of capacitive performance benefits result from a well-developed interconnected hierarchical structure and provides more electrochemical active site, facilitating the penetration and diffusion of electrolyte. This study provides a general guidance to develop different morphologies of electrode materials for supercapacitor device.

1 Introduction

The continuous development and innovation of humanity promote the increasing demand for energy, resulting in the poverty of non-renewable energy

resources. Therefore, developing a green energy storage devices with high utilization efficiency has become urgent and necessary. In this regard, various types of energy storage devices including lead-acid/ion battery, supercapacitors (SCs) and fuel cells, have

Gaodan Luo and Guiqiang Diao have contributed equally to this work.

Address correspondence to E-mail: suxiaohui4336@126.com

caused the extensive concern. Among them, SCs with high power density, environmental friendliness, low cost and long cycle life (used more than 10^5 times) have been known as the most potential energy storage devices [1–3] for potential application prospect in automobile, military, portable electronic equipment and others fields [4, 5]. The SCs can be divided into two mechanisms, one is pseudocapacitors which exhibit faradic reaction on the surface or subsurface of the electrodes, and the other is electrochemical double-layer capacitors (EDLCs) produced by charge separation [6–8].

Transition metal oxides including RuO_2 [9], NiO [10], Co_3O_4 [11] and MnO_2 [12, 13] can meet the requirement of modern devices for high power density [14, 15]. Among them, MnO_2 exhibits many advantageous properties, such as the abundant resources, low costs, pollution-free, and high theoretical specific capacitance (1370 F g^{-1}) [16, 17], which have been considered to be the promising candidate electrode materials for pseudocapacitors. However, for pristine MnO_2 material has poor intrinsic conductivity and relatively poor electrochemical stability, which reduces its importance in supercapacitor applications. In order to address these problems, one effective strategy is to combine it with conductive carbon material to realize self-supported and the binder-free growth [18]. To this end, fabricating carbon structures on free-standing substrates like CFP has become the favorable method for supercapacitors owing to its several advantages such as reasonable cost, excellent chemical stability, and good electrical conductivity [19].

Another effective way to improve electrochemical performance is to design manganese dioxide nanostructured materials with unique morphologies, such as nanoflowers, nanowires, nanosheets, nanorods and so forth [20–23]. At present, many methods like hydrothermal, microwave, and electrodeposition [24–26], have been applied for the preparation of MnO_2 nanostructured materials. Among these synthesis methods, hydrothermal method has drawn the great attention owing to its advantageous such as controllable, simple, and effective. For example, Mohamed [27] et al. prepared MnO_2 electrode material by the hydrothermal method, which generated a high specific capacitance of 175.51 F g^{-1} at 0.5 A g^{-1} . Xia [28] et al. developed a hydrothermal method to successfully synthesize MnO_2 as supercapacitor material in a temperature range of 130 to

$170 \text{ }^\circ\text{C}$. According to previous literature reports, it can be known that the electrochemical properties of MnO_2 mainly determine by surface area, morphology and crystal phase [29]. Therefore, extensive efforts are committed to design MnO_2 nanostructure with ideal morphologies by regulating the synthesis conditions [30–32]. For example, Li et al. fabricated nanosheet assembly with various structures MnO_2 via Fe regulation process, which show a specific capacitance of 210 F g^{-1} at 0.3 A g^{-1} [33]. Bai et al. synthesized cauliflower-like MnO_2 and needle-like MnO_2 electrodes by changing the synthesis conditions, needle-like MnO_2 exhibits better electrochemical properties than cauliflower like particles [34]. Recently, a facile design of the hierarchical structure has been developed, which can provide more active centers and shorten the diffusion distance for ions between electrolyte and electrode, resulting in the excellent capacitive performance. Hence, constructing the morphology of MnO_2 with good electrochemical properties is of great significance for their exploitation in the field of energy storage.

Hence, the hierarchical porous Co-doped MnO_2 nanoflowers entwined with nanowires structure were successfully synthesized on CFP via a facile hydrothermal reaction. The optimal as-prepared electrode (Co- MnO_2 /CFP-1) achieve a relatively high-rate capability of 57% at 8 A g^{-1} , which was 27 times higher than MnO_2 without Co doping (MnO_2 /CFP). The effect of different doping content on crystal phase, morphology and capacitive performance of as-prepared MnO_2 materials were analyzed and interpreted in detail in this research.

2 Experimental section

2.1 Materials

Potassium permanganate (KMnO_4 , Guangzhou Chemical Reagent Co. Ltd.), Sodium dodecyl sulfate ($\text{C}_{12}\text{H}_{25}\text{SO}_4\text{-Na}$, SDS, Guangzhou Chemical Reagent Co. Ltd.) and Cobalt (II) acetate ($\text{C}_4\text{H}_6\text{CoO}_4$, Guangzhou Chemical Reagent Co. Ltd.). All the reagents are used without further purification in this study.

2.2 Material synthesis

CFP was washed in acetone, 0.3 M HNO₃ solution and deionized water by ultrasonic cleaner, respectively. Figure 1 shows a schematic diagram of the synthesis of the electrodes. Briefly, SDS (0.08 g) was dispersed to 20 ml deionized (DI) water, and then 15 ml of 0.084 g mL⁻¹ KMnO₄ solution was drip into it. Finally, different amounts of C₄H₆CoO₄, 0.0, 1.5, and 5.5 mmol were dissolved into the obtained mixed solution while stirring constantly for 15 min, respectively, and then the CFP (1 × 1.5 cm) was placed into the obtained homogeneous solutions and transferred to a 50 mL Teflon-lined autoclave that was maintained in the oven at 140 °C for 12 h. To have a better comparison, MnO₂ was fabricated with the same steps as above without adding cobalt acetate. The result samples were taken out and rinsed by deionized water for several times, then dried at 80 °C for 4 h in an oven. The weight of active material was calculated by subtraction. These products were separately abbreviated as MnO₂/CFP (0.0 mmol C₄H₆CoO₄), Co-MnO₂/CFP-1 (1.5 mmol C₄H₆CoO₄), and Co-MnO₂/CFP-2 (5.5 mmol C₄H₆CoO₄), respectively.

2.3 Characterization

The crystal structure of the as-prepared electrode materials was determined and analyzed by German Bruker D8 X-ray diffraction (XRD) equipment. The morphology was analyzed by scanning electron microscopy (SEM, S3400 series, Hitachi) and transmission electron microscopy (TEM, HT7700, Hitachi). The surface areas, pore volume and pore size distribution was evaluated via brunner emmet teller (BET)

surface area analyzer (Quantachrome NOVA2200e). Samples were degassed at 100 °C for 11 h before measurement.

2.4 Electrochemical measurements

The cyclic voltammetry (CV), galvanostatic charge/discharge (GCD) and electrochemical impedance spectroscopy (EIS) of the as-prepared electrode materials were measured on an electrochemical workstation (PGSTAT302N) using a conventional three-electrode device in 1.0 M Na₂SO₄ aqueous solution, including working electrodes (the as-prepared MnO₂ samples), Pt plate counter electrode and Hg/HgCl reference electrode. The specific capacitance of the samples was derived from the GCD curves based on the following equation:

$$C = \frac{I\Delta t}{m\Delta v} \quad (1)$$

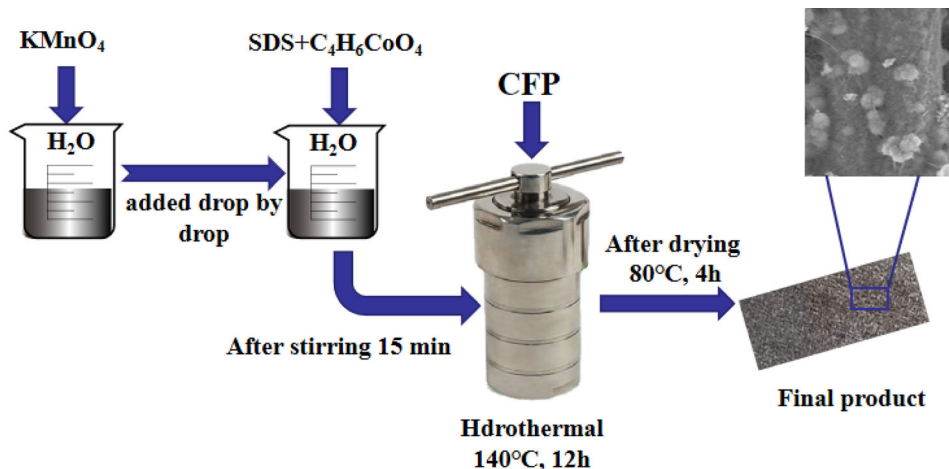
I, Δt, m and ΔV corresponded to the constant discharge current (A), the total discharge time (s), the loading mass of the as-prepared material (g) and the potential window of electrode (V), respectively.

3 Results and discussion

3.1 Structure analyses

The crystal phase of as-obtained MnO₂ (scraped from CFP) electrode materials was characterized by XRD in Fig. 2. The MnO₂/CFP and Co-MnO₂/CFP-1 showed the similar diffraction peaks at 12.4°, 24.8°, 37.4 and 66.4° could be assigned to (001), (002), (111), and (020) planes, respectively, which was indexed as

Fig. 1 The preparation procedure of the MnO₂ composite electrode by hydrothermal method



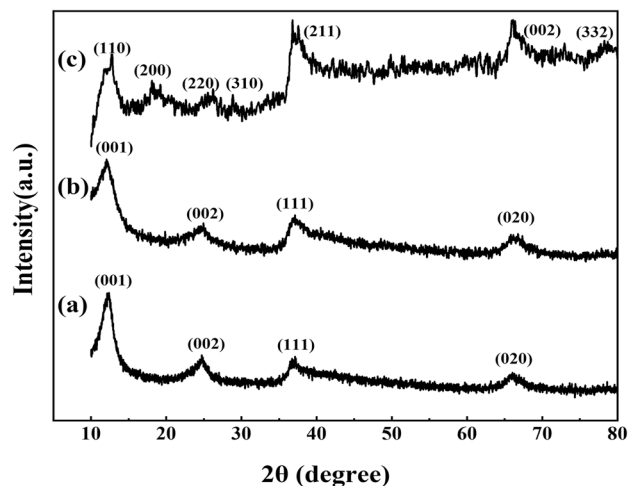


Fig. 2 XRD patterns of MnO₂/CFP (a), Co-MnO₂/CFP-1 (b) and Co-MnO₂/CFP-2 (c)

δ -MnO₂ (JCPDS 42–1317) [35]. The main peaks of Co-MnO₂/CFP-2 in Fig. 2c were located at 12.4°, 17.6°, 28.6°, 37.5° and 64.8°, which could be assigned to (110), (200), (310), (211), and (002) of α -MnO₂ phase (JCPDS 44-0141) [36, 37]. As seen from Fig. 2b and c, no diffraction signals from Co species were detected in the XRD patterns of Co-MnO₂/CFP-1 and Co-MnO₂/CFP-2, revealing that no crystallized cobalt oxide was formed or the content of Co was low in the samples. The characteristics of the XRD patterns demonstrated that the phase could be changed from δ -MnO₂ to α -MnO₂ with the increasing of Co content. From XRD, the average crystallite size (D_c) of obtained MnO₂ particles was calculated according to the Scherrer equation:

$$D_c = \frac{K\lambda}{\beta \cos\theta},$$

where the K , β , λ , θ correspond to a constant, full-width half maximum (FWHM), the wavelength of X-ray and the diffraction angle, respectively. The D_c of obtained MnO₂/CFP, Co-MnO₂/CFP-1 and Co-MnO₂/CFP-2 particle was 8.7, 7.1, and 11.7 nm, respectively.

The surface morphologies and chemical composition of the as-obtained MnO₂ electrodes were analyzed by SEM. From Fig. 3a and b, the undoped MnO₂ showed a mix nanosheet network and nanoflowers-like structure. Some nanosheets aggregate together to form nanoflowers-like structure and some of them internet with each another to grow compactly and uniformly on the surface of CFP. As

seen from Fig. 3c and d, the growth of nanosheets was suppressed, shows an interesting structure comprising hybrid nanoflowers entwined with nanowires structure. The nanowires wrapped around nanoflowers to form a well-developed interconnected hierarchical structure and provides more electrochemical active site, facilitating the penetration and diffusion of electrolyte, which was conducive to the improvement of electrochemical behavior of electrode materials. The samples of Co-MnO₂/CFP-2 is shown in Fig. 3e and f, the nanoflowers-like MnO₂ structure disappear, and only the disorganized nanorods was deposited onto the surface of CFP. The main components of the material surface were analyzed by EDS element scanning, the atomic percentage of the constituent elements Co, O, K, C and Mn for as-prepared materials were calculated from the EDS spectrum in Table 1. It could see that the distribution of C element was so weak, indicate that a large amount of MnO₂ was grown on the surface of CFP. In addition, the appearance of the K element was due to the potassium permanganate, which used in reaction process. According to SEM patterns and EDS, it was confirmed that the morphology transformation of MnO₂ from nanoflowers-like structure to disorganized nanorods-like structure could be completed by adjusting the content of Co.

Figure 4a–c display a schematic illustration of the changes in morphologies of the MnO₂ nanostructures. The corresponding TEM images are performed in Fig. 4d–f. According to the “Ostwald ripening process” [38], with the high temperature decomposition of KMnO₄, large initial particles were gathered together to form thin nanosheets, and then partially aggregation of MnO₂ nanosheets occurs, resulting in the formation of nanoflowers-like MnO₂ structure as shown in Fig. 4d, which were uniform in size with an average diameter of ~ 130 nm. As the addition of Co, it may conducive to the formation of nanowires, resulting in the hybrid nanoflowers entwined with nanowires structure, with a diameter of ~ 70 nm. When the amount of C₄H₆CoO₄ was added to 5.5 mmol, the dissolution of MnO₂ nanosheets may occur due to the increase of Co content, and then form MnO₂ nanorods by oriented growth [21], with an average diameter of ~ 110 nm. Thus, the morphologies of MnO₂ vary with the content of Co. The high-resolution TEM (HRTEM) images of the as-prepared MnO₂ were found in inset of Fig. 4d–f, in which the lattice fringes with the spacing

Fig. 3 SEM images of MnO₂/CFP (a, b), Co-MnO₂/CFP-1 (c,) and Co-MnO₂/CFP-2 (e, f)

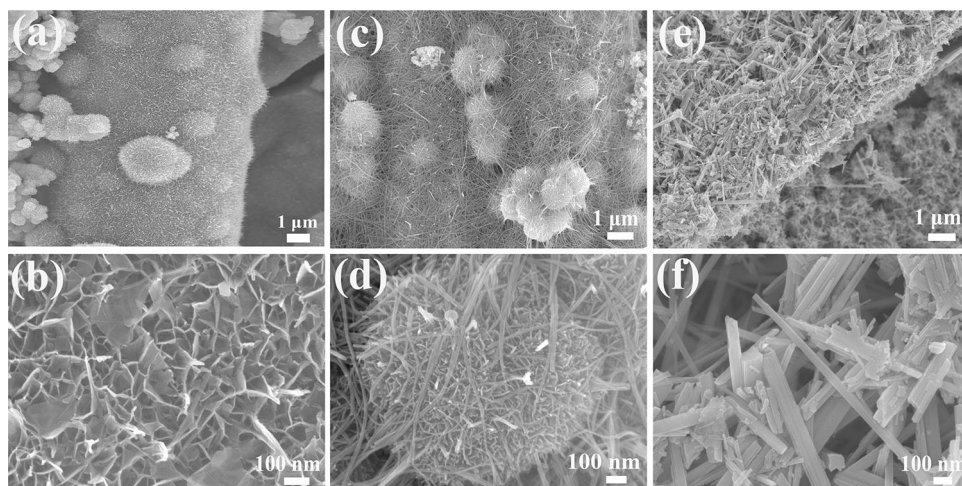
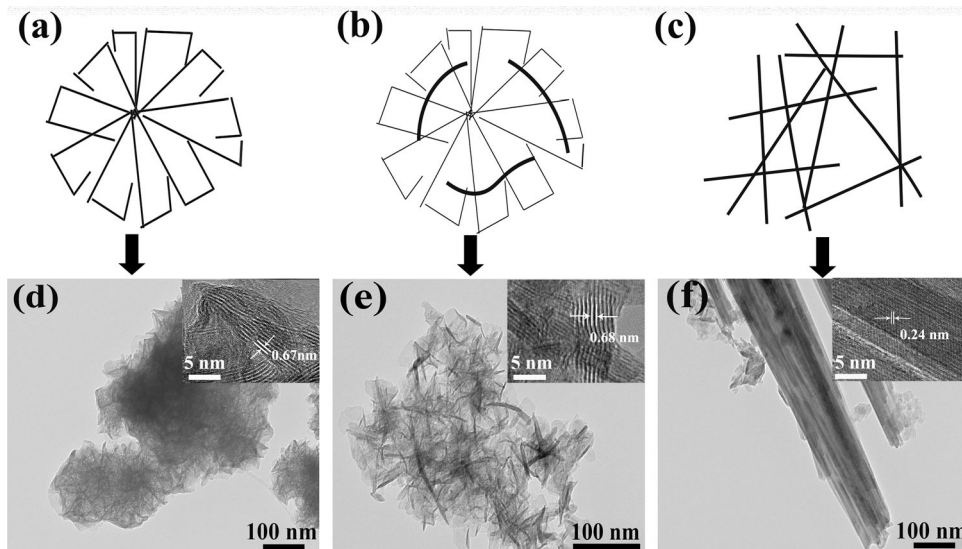


Table 1 Atomic ratio of element Mn, Co, K, O and C for MnO₂/CFP, Co-MnO₂/CFP-1 and Co-MnO₂/CFP-2

Atomic%	Co	Mn	O	K	C
MnO ₂ /CFP	0	24.8	73.4	1.08	0.69
Co-MnO ₂ /CFP-1	0.13	22.8	71.9	4.28	0.82
Co-MnO ₂ /CFP-2	1.46	27.1	66.3	3.84	1.28

with a hysteresis loop observed at relatively high pressure, proving the existence of mesoporous structure [39]. Furthermore, the specific surface area of Co-MnO₂/CFP-1 (218 m² g⁻¹) increased significantly compared with that of MnO₂/CFP (39 m² g⁻¹) and Co-MnO₂/CFP-2 (113 m² g⁻¹) in Fig. 5a. The pore volumes of MnO₂/CFP, Co-MnO₂/CFP-1 and Co-MnO₂/CFP-2 were calculated to be 0.16, 0.63 and

Fig. 4 Schematic illustrations (a–c), the corresponding TEM (d–f) and HRTEM (in inset of Fig. 4d–f) images of MnO₂/CFP, Co-MnO₂/CFP-1 and Co-MnO₂/CFP-2, respectively



of 0.67 and 0.68 nm could be assigned to (001) planes of δ-MnO₂, and the lattice fringe with the spacing of 0.24 nm could be indexed as the (211) of α-MnO₂.

Nitrogen adsorption-desorption isotherms and porosity of the as-obtained material are shown in Fig. 5a. The structural parameters of the prepared materials are shown in Table 2. All of the materials could be classified as type-IV adsorption isotherm

0.21 cm³ g⁻¹, respectively. Among them, Co-MnO₂/CFP-1 with the largest pore volume was conducive to provide the ion transport path. The Barrett-Joyner-Halenda (BJH) analysis is shown in Fig. 5b, the pore size of MnO₂/CFP, Co-MnO₂/CFP-1 and Co-MnO₂/CFP-2 were determined to be 3.8, 3.4, and 4.9 nm, respectively, which revealed again the mesoporous structure of the samples. Furthermore, the SEM

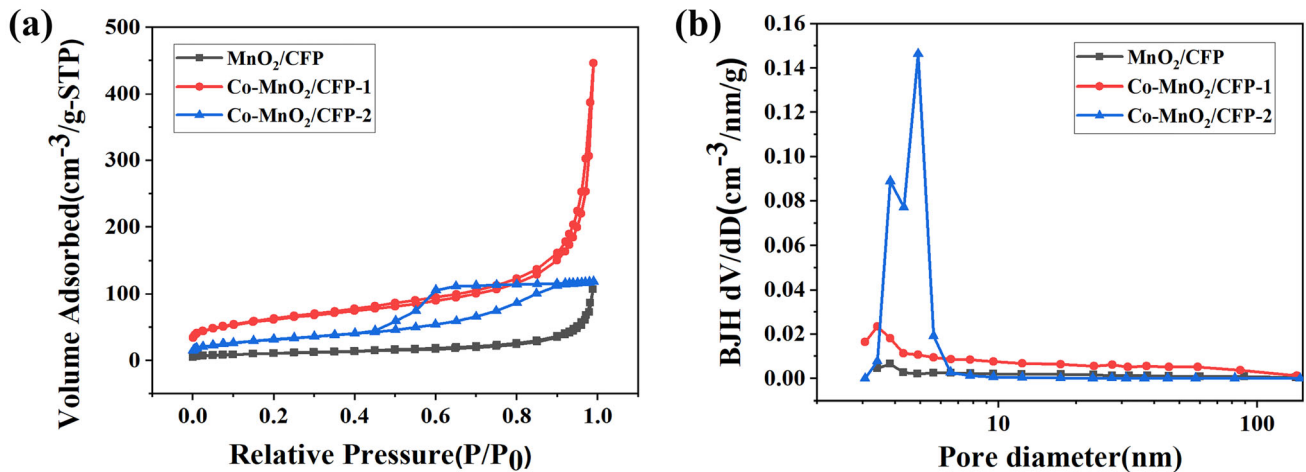


Fig. 5 Nitrogen adsorption-desorption isotherms (a) and BJH pore size distribution curves of MnO₂/CFP, Co-MnO₂/CFP-1 and Co-MnO₂/CFP-2 (b)

Table 2 The specific surface areas, pore volumes and pore size parameters of MnO₂/CFP, Co-MnO₂/CFP-1 and Co-MnO₂/CFP-2

	Specific surface areas(m ² g ⁻¹)	Pore volumes(cm ³ g ⁻¹)	Pore size (nm)
MnO ₂ /CFP	39	0.16	3.8
Co-MnO ₂ /CFP-1	218	0.61	3.4
Co-MnO ₂ /CFP-2	113	0.23	4.9

images (Fig. 3c, d) and BET results strongly showed that the Co-MnO₂/CFP-1 had a well-developed interconnected hierarchical structure and relatively high surface area which facilitated the diffusion of electrolyte ions/electrons and offered more electroactive sites to participate in the charge-discharge process [40].

3.2 Electrochemical evaluation

The electrochemical behavior of as-obtained electrode materials were investigated by the CV measurements. In Fig. 6a, a comparative study of the CV curves of different electrode materials at the scan rates of 50 mV s⁻¹ in a potential window of 0–1 V (vs. SCE) was observed. The enclosed area of the CV curves could suggest its specific capacity, the larger the closed area was, the higher the corresponding capacity was. The largest enclosed area was possessed by the Co-MnO₂/CFP-1 electrode compared with MnO₂/CFP and Co-MnO₂/CFP-2, demonstrating the higher capacitance behavior of the Co-MnO₂/CFP-1 electrode, which strongly benefits from the appropriate Co doping content. Figure 6b–d exhibit the CV curves for MnO₂/CFP, Co-MnO₂/CFP-1 and Co-MnO₂/CFP-2 at various scan rates of 5, 20, 50,

and 100 mV s⁻¹. Figure 6b and c present almost rectangular shapes when the scan rates at 5 and 20 mV s⁻¹, demonstrating the good capacitive behavior [41]. As the scanning rate increase from 50 to 100 mV s⁻¹, its shapes deviate from rectangular, which was mainly because that electrolyte ions could not reach the interior of the electrode due to the insufficient time, and the using efficiency of active substances was reduced, leading to the deviation of the curves [42].

To analyze the electrochemical behaviors of the as-obtained electrodes more intuitively, GCD experiments were characterized in the potential window between 0–1 V versus SCE. Figure 7a displays a comparative study of GCD profile for as-prepared electrode materials at the current density of 1 A g⁻¹. Distinctly, the quasi-triangle shape of charge-discharge curves further confirmed the good electrochemical reversibility of as-prepared electrodes. As expected, the specific capacitance of Co-MnO₂/CFP-1 was 161 F g⁻¹ according to Eq. (1), exhibiting 40% increased over MnO₂/CFP (115 F g⁻¹). In contrast, Co-MnO₂/CFP-2 had only 25 F g⁻¹, such a low specific capacitance was probably owing to the disorganized nanorods, which was not conducive to the effective electrolyte access into the electrode. Above

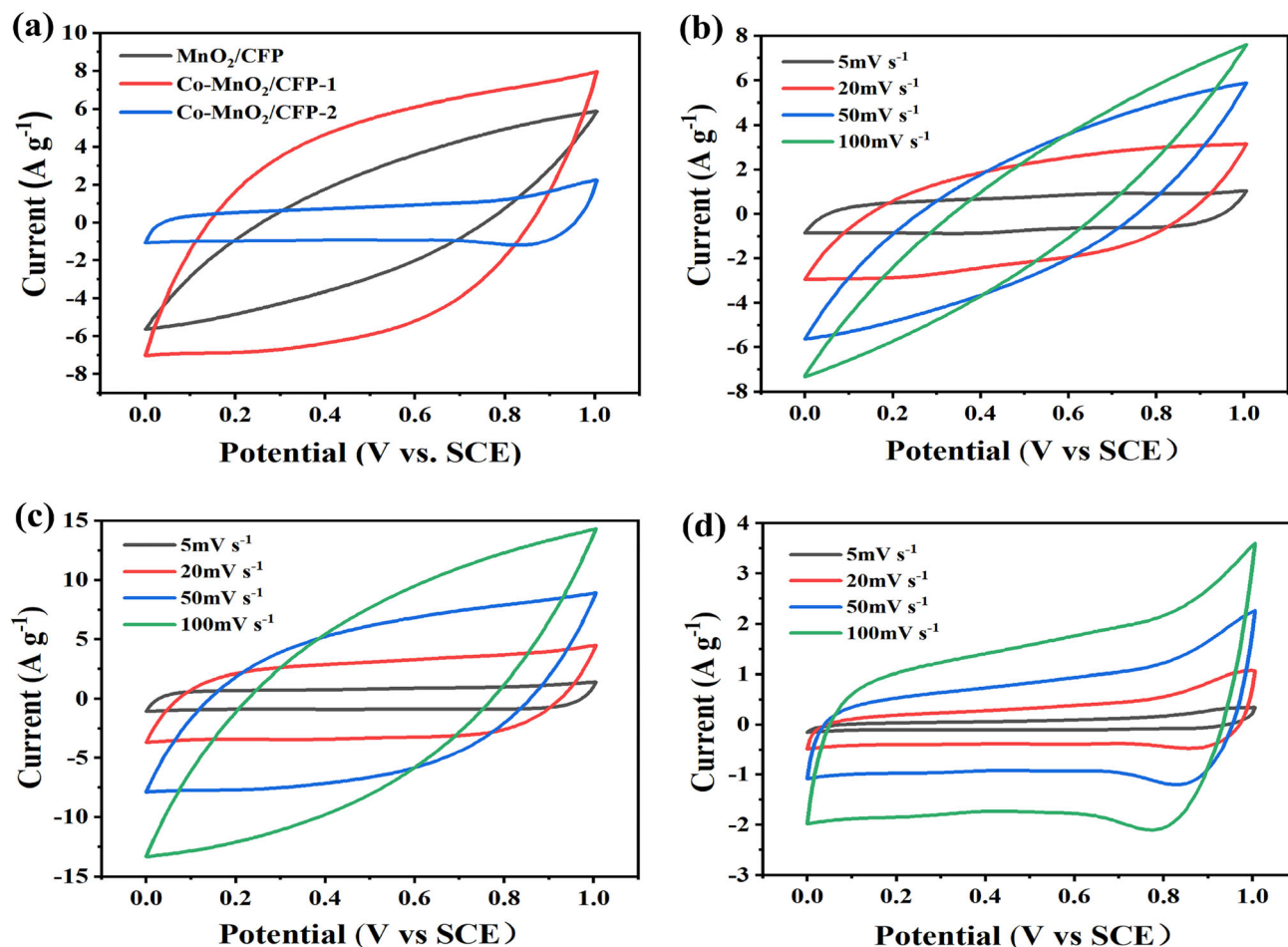


Fig. 6 CV curves of MnO₂/CFP, Co-MnO₂/CFP-1 and Co-MnO₂/CFP-2 samples at 50 mV s⁻¹ (a), CV curves of MnO₂/CFP, Co-MnO₂/CFP-1 and Co-MnO₂/CFP-2 at different scan rates, respectively (b–d)

observed changes in these samples were consistent with the CV analysis. Furthermore, the relationship between the specific capacitance and current densities ranging from 0.5 to 8 A g⁻¹ and the specific charge–discharge behaviors of MnO₂/CFP, Co-MnO₂/CFP-1 and Co-MnO₂/CFP-2 are shown in Fig. 7b–e. The specific capacitances of all samples increased significantly with the decrease of current densities, it is mainly because that the slowly current accumulating process facilitate fully contact of electroactivity sites on the electrode, thereby leading to the higher capacitances [43]. Impressively, the Co-MnO₂/CFP-1 achieved a prominent performance in terms of supercapacitor behavior with an outstanding rate performance of 57% when the current density ranging from 1 to 8 A g⁻¹. In contrast, only 2.1% of the capacity retention for MnO₂/CFP at 8 A g⁻¹. The above results showed that the capacitance and rate

performance could be improved owing to the adding of appropriate Co content, which was ascribed to the optimized hierarchical porous nanoflowers entwined with nanowires structure, the high surface area and porosity effectively facilitate the transport for electron in the electrode.

The EIS was performed at open circuit voltage to estimate the influence of Co element for the detail resistance of as-prepared electrodes, the corresponding results are observed in Fig. 8. Notably, all of the Nyquist plots consisted of a distorted semicircle in the high frequency, following by a nearly vertical line at low frequency. The conductivity of the as-prepared electrode materials was measured by equivalent series resistance (R_s), which originated from the intrinsic resistance of current collector, ionic resistance of electrolyte and contact resistance at the interface of electrode and electrolyte [34, 44], obtaining from the

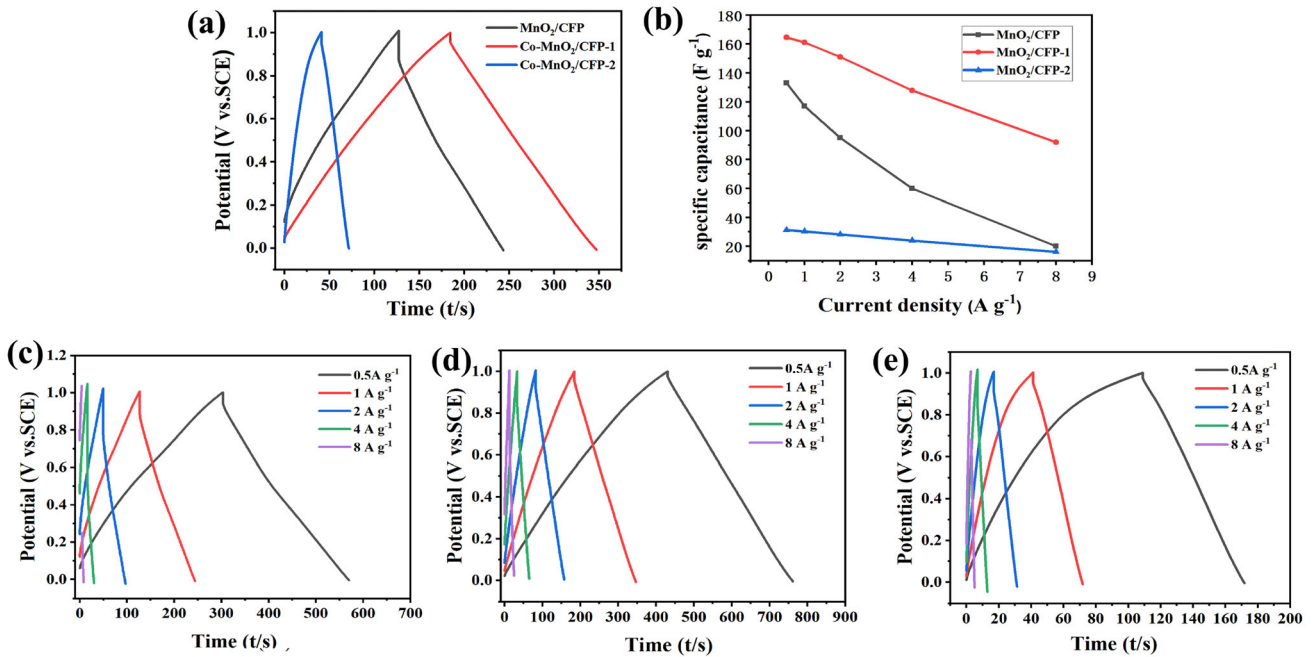


Fig. 7 Charge–discharge curves of MnO₂/CFP, Co-MnO₂/CFP-1 and Co-MnO₂/CFP-2 at 1 A g⁻¹ (a), The relationship between the specific capacitance and current densities ranging from 0.5 to 8 A

g⁻¹ (b) and charge–discharge curves of MnO₂/CFP, Co-MnO₂/CFP-1 and Co-MnO₂/CFP-2 at different current densities (c–e)

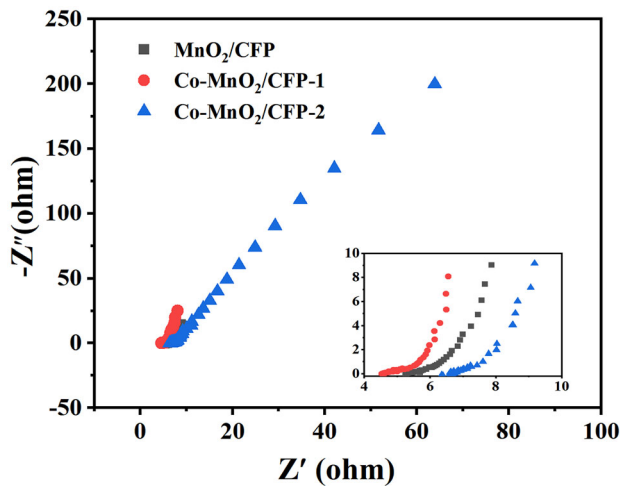


Fig. 8 Nyquist plots of MnO₂/CFP, Co-MnO₂/CFP-1 and Co-MnO₂/CFP-2

intercept at the real axis. According to Fig. 8, the R_s values of MnO₂/CFP, Co-MnO₂/CFP-1, and Co-MnO₂/CFP-2 are found to be 5.53, 4.22, and 6.61 Ω, respectively, the Co-MnO₂/CFP-1 electrode exhibited a higher electrical conductivity than other electrodes. The slope of straight line within the low frequency region represented the ions migration within the as-prepared material. Obviously, the larger slope of the

Co-MnO₂/CFP-1 was larger than that of other electrodes. Among these as-prepared materials, the Co-MnO₂/CFP-1 had the minimum R_s and the largest slope, which was conducive to ion diffusion and charge transfer, and further demonstrated that the electrochemical performance was superior to others. In terms of microstructure, the R_s value of hierarchical porous nanoflowers entwined with nanowires structure was smaller than that of nanoflowers and disorganized nanorods structures, suggesting that the hierarchical porous structure could provided more shorter transport path for ions in electrolyte.

The cyclic performance of the MnO₂/CFP and Co-MnO₂/CFP-1 materials was evaluated by sequential charge–discharge cycling. As shown in Fig. 9a, the specific capacitance of Co-MnO₂/CFP-1 decreased slightly and exhibited a higher capacitive retention of 98% at the current density of 4 A g⁻¹ after 10,000 cycles, showing an excellent cyclic stability of the Co-MnO₂/CFP-1 electrode. In contrast, the MnO₂/CFP had a relatively low cyclic stability with about 88% capacitance retention after 10,000 cycles. Figure 9b and c present the Nyquist plots of the MnO₂/CFP and Co-MnO₂/CFP-1 before and after 10,000 cycles. After 10,000 cycles, the Co-MnO₂/CFP has an increase of R_s from 5.75 to 9.39 Ω, but only 4.22

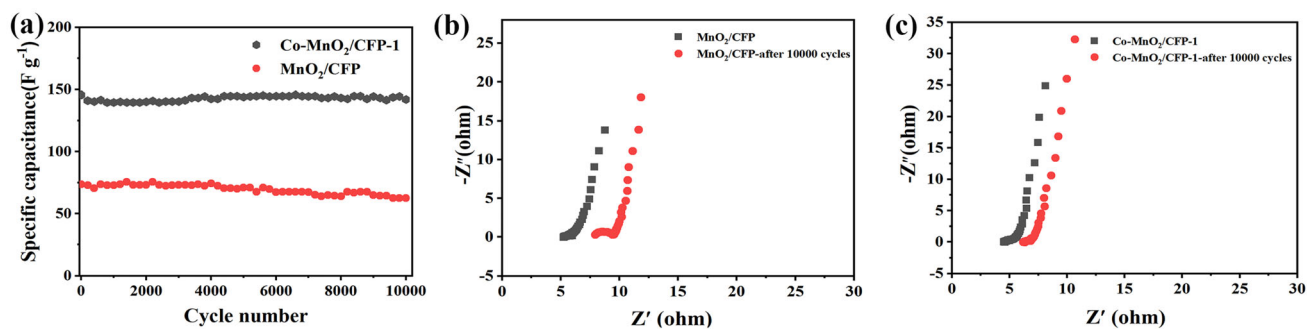


Fig. 9 Cycling stability of MnO_2/CFP and $\text{Co-MnO}_2/\text{CFP-1}$ at a current density of 4 A g^{-1} (a), Nyquist plots of MnO_2/CFP and MnO_2/CFP after 10,000 cycles (b), Nyquist plots of $\text{Co-MnO}_2/\text{CFP-1}$ and $\text{Co-MnO}_2/\text{CFP-1}$ after 10,000 cycles (c)

6.20Ω was observed for $\text{Co-MnO}_2/\text{CFP-1}$. These EIS analysis further proved the excellent cycle stability of the $\text{Co-MnO}_2/\text{CFP-1}$ electrode, the unique hierarchical porous nanoflowers entwined with nanowires structure could effectively adjust the volume expansion of as-prepared MnO_2 electrode during redox process and ensured the required cycle stability [45].

4 Conclusion

In conclusion, MnO_2 with different morphologies was fabricated on carbon fiber papers using a hydrothermal method by adjusting the amount of Co doping. It was found that the optimal $\text{Co-MnO}_2/\text{CFP-1}$ electrode showed the excellent electrochemical properties due to its unique hierarchical porous nanoflowers entwined with nanowires structure, providing sufficient active sites and more shorter transport path for ions in electrolyte. The SCs based on $\text{Co-MnO}_2/\text{CFP-1}$ showed a high specific capacity values of 161 F g^{-1} at 1 A g^{-1} , and the capacitance retention was up to 57% as the current density ranging from 1 to 8 A g^{-1} . In addition, The $\text{Co-MnO}_2/\text{CFP-1}$ exhibited excellent cycle stability of 98% after 10,000 cycles. These work provided more insight for the synthesis of electrode materials with different morphologies in energy storage.

Acknowledgements

This work was supported by National Natural Science Foundation of China (21905054).

Author contributions

All authors have contributed to the study conception and design. GL and GD: Material preparation, Experiment, Data analysis, Writing. QH: Experiment, Analyzing Writing. SH and DD: Writing-review & editing. XS: Supervision, Data curation, Guiding. All authors read the paper and commented on the text. The authors have read and approved the final manuscript.

Funding

National Natural Science Foundation of China, 21905054, Xiaohui Su

Data availability

The datasets generated during and/or analyzed during the current study are available from the corresponding author on reasonable request.

Declarations

Competing interests The authors declared that they have no conflicts of interest to this work. We declare that we do not have any commercial or associative interest that represents a conflict of interest in connection with the work submitted.

References

1. R. Zhong, M. Xu, N. Fu, R. Liu, A. Zhou, X. Wang, Z. Yang, *Electrochim. Acta.* **136209**, 348 (2020)
2. N. Yu, J. Zhao, R. Liu, F. Li, Y. Du, Z. Yang, *ACS Omega* **15904–15911**, 4 (2019)

3. H.K. Chang, Y. Cheol-Min, A.K. Yoong, S.Y. Kap, *Appl. Surf. Sci.* **143693**, 497 (2019)
4. D. Tang, Y. Luo, W. Lei, Q. Xiang, W. Ren, W. Song, K. Chen, J. Sun, *Appl. Surf. Sci.* **862–871**, 462 (2018)
5. Y. Huang, Y. Li, G. Zhang, W. Liu, D. Li, R. Chen, F. Zheng, H. Ni, *J. Alloy. Comp.* **603–611**, 778 (2019)
6. W. Wei, X. Cui, W. Chen, D.G. Ivey, *Chem. Soc. Rev.* **1697–1721**, 40 (2011)
7. R.S. Kate, S.A. Khalate, R.J. Deokate, *J. Alloy. Comp.* **89–111**, 734 (2018)
8. X. Shi, S. Zheng, Z.S. Wu, X. Bao, *J. Energy. Chem.* **25–42**, 27 (2018)
9. R. Li, L. Yu, S. Li, J.R. Luo, J. Zhao, *Electrochim. Acta.* **52–59**, 284 (2018)
10. T.F. Yi, J. Mei, B. Guan, P. Cui, S. Luo, Y. Xie, Y. Liu, *Ceram. Int.* **421–429**, 46 (2020)
11. Y. Zhang, Y. Hu, Z. Wang, T. Lin, X. Zhu, B. Luo, L. Wang, *Adv. Funct. Mater.* **2004172**, 30 (2020)
12. Z. Huang, Y. Song, D. Feng, Z. Sun, X. Sun, X. Sun, *ACS Nano* **3557–3567**, 12 (2018)
13. P.E. Saranya, S. Selladurai, *New. J. Chem.* **7441–7456**, 43 (2019)
14. M. Manuraj, J. Chacko, K.N.N. Unni, R.B. Rakhi, *J. Alloy. Compd.* **155420**, 836 (2020)
15. B.C. Kim, C.J. Raj, W. Cho, W. Lee, H.T. Jeong, K.H. Yu, *J. Alloy. Compd.* **491–497**, 617 (2014)
16. Q. Zhang, X. Wu, Q. Zhang, *J. Electroanal. Chem.* **108–115**, 837 (2019)
17. J. Zhang, Y. Wei, Q. Yan, L. Guo, Z. Xie, J. Yang, W. He, Z. Qi, X. Cao, P. Zhao, H. Pan, K. Li, J. Zhang, X. Zhao, P. Li, K.W. Zhang, *J. Power. Sources.* **227616**, 450 (2020)
18. S. He, C. Zhang, C. Du, C. Cheng, W. Chen, *J. Power. Sources.* **226701**, 434 (2019)
19. W. Ko, Y. Liu, J. Lai, C. Chung, K. Lin, *ACS. Sustain. Chem Eng.* **669–678**, 7 (2018)
20. Y. Zhao, Y. Meng, P. Jiang, *J. Power. Sources.* **219–226**, 259 (2014)
21. F.N.I. Sari, P.R. So, J.M. Ting, *J. Am. Ceram. Soc.* **1642–1652**, 100 (2017)
22. A. Xi, W. Yu, J. Yi, G. Tan, H. Ren, C. Liu, *J. Electroanal. Chem.* **25–31**, 839 (2019)
23. P. Sun, H. Yi, T. Peng, Y. Jing, R. Wang, H. Wang, X. Wang, *J. Power Sources.* **27–35**, 341 (2017)
24. H. Shen, Y. Zhang, X. Song, Y. Liu, H. Wang, H. Duan, X. Kong, *J. Alloy. Compd.* **926–933**, 770 (2019)
25. F. Wang, J. Zheng, G. Li, J. Ma, C. Yang, Q. Wang, *Mater. Chem.* **121–126**, 215 (2018)
26. M. Zhang, Y. Chen, D. Yang, J. Li, *J. Energy. Storage.* **101363**, 29 (2020)
27. K. Mohamed, A. Manikandan, M. Mahendiran, J. Madhavana, M. Antony, M. Mohamed, T. Maiyalagan, *Ceram. Int.* **6222–6233**, 46 (2020)
28. A. Xia, W. Yu, J.G. Tan, H. Yi, C. Ren, *J. Electroanal. Chem.* **25–31**, 839 (2019)
29. W. Xing, F. Li, Z.F.G. Yan, Q. Lu, *J. Power Sources* **134**, 324–330 (2004)
30. B. He, G. Cheng, S. Zhao, X. Zeng, Y. Li, R. Yang, M. Sun, L. Yu, *J. Solid, State Chem.* **305–311**, 269 (2019)
31. T. Su, B. Zhao, B. Fan, H. Li, R. Zhang, *J. Solid. State. Chem.* **192–198**, 273 (2019)
32. M. Toupin, T. Brousse, D. Bélanger, *Chem. Mater.* **3184–3190**, 16 (2004)
33. J. Li, B. Hu, P. Hu, X. Shang, W. Jiang, K. Xu, J. Liu, *Appl. Surf. Sci.* **1415**, 542 (2021)
34. X. Bai, X. Tong, Y. Gao, W. Zhu, C. Fu, J. Ma, T. Tan, C. Wang, Y. Luo, H. Sun, *Electrochim. Acta.* **525–533**, 281 (2018)
35. Z. Fan, M. Xie, X. Jin, J. Yan, T. Wei, *J. Electroanal. chem.* **191–195**, 659 (2011)
36. N. Bose, V. Sundararajan, T. Prasankumar, S.P. Jose, *Mater. Lett.* **128457**, 278 (2020)
37. R.A. Davoglio, G.J. Cabello, F. Marco, S.R. Biaggio, *Electrochim. Acta.* **428–435**, 261 (2018)
38. B.X. Li, G.X. Rong, Y. Xie, L.F. Huang, C.Q. Feng, *Inorg. Chem.* **6404–6410**, 45 (2006)
39. S.J. Gregg, K.S. Sing, W.H.W. Salzberg, *J. electrochem. soc.* **279C**, 114 (1967)
40. Q. Cheng, J. Tang, J. Ma, H. Zhang, N. Shinya, L.C. Qin, *Carbon* **2917–2925**, 49 (2011)
41. Y. Zhang, X. Yuan, W. Lu, Y. Lu, J. Zhu, T. Chou, *Chem. Eng. J.* **525–532**, 368 (2019)
42. X. Lang, A. Hirata, T. Fujita, M. Chen, *Nat. nanotechnol.* **232–236**, 6 (2011)
43. C. Wang, F. Li, H. Qu, Y. Wang, X. Yi, Y. Qiu, Z. Zou, Y. Luo, B. Yu, *Electrochim. Acta.* **35–41**, 158 (2015)
44. Z. Lei, N. Christov, X.S. Zhao, *Energ. Environm. Sci.* **1866–1873**, 4 (2011)
45. F.L. Yu, C. Xu, X. Lou, *Energy Environ. Sci.* **862–866**, 9 (2016)

Publisher's Note Springer Nature remains neutral with regard to jurisdictional claims in published maps and institutional affiliations.